2024 IEEE/RSJ International Conference on Intelligent Robots and Systems (IROS)
October 14-18, 2024. Abu Dhabi, UAE

Development of Permanent Magnet Elastomer-based Tactile Sensor with Adjustable Compliance and Sensitivity

Devesh Abhyankar*, Yushi Wang*, *Member, IEEE*, Yuhiro Iwamoto, *Member, IEEE*
Shigeki Sugano, *Fellow, IEEE*, Mitsuhiro Kamezaki, *Member, IEEE*

***Abstract*— Tactile sensors are crucial in robotics as they enable robots to perceive and interact with their environment through touch, akin to the human sense of touch. Adjustable sensors that can adapt to various tasks by functional or structural modification have not been extensively explored. In terms of sensing adjustability of a sensor, two important aspects are the sensor's sensitivity and compliance. This paper proposes a novel design for an adjustable compliance and sensitivity sensor composed of a silicone base, a permanent magnet elastomer (PME), and a printed circuit board (PCB) with magnetic transducers installed. Its adjustability is achieved by varying the pneumatic pressure. This paper presents the design, manufacturing process, and experimental characterization of such an adjustable compliance and sensitivity sensor. This paper thoroughly investigates how altering the pressure of the sensor influences its sensing properties. The results show that it can achieve adjustability in all three axes. For the current design, the sensitivity can be varied from 0.093 to 0.125 mT/N (34.41%), 0.089 to 0.13 mT/N (31.54%), and 0.169 to 0.45 mT/N (62.44%) in the X-, Y-, and Z-axis, respectively. The deformation it undertakes varies from 3.20 to 3.79 mm (18.44%), indicating the compliance change.**

I. Introduction

Traditionally, the robotics industry and research community mainly focused on industrial robots, but as demand has grown and technology has advanced, there has been a notable shift towards developing general-purpose humanoid robots [1]. In contrast to industrial robots, which are designed for predefined environments and specific tasks, general-purpose robots are engineered to operate in unstructured environments and handle a broader range of tasks [2]. Therefore, it is essential to develop the capability to fine-tune a robot's sensing abilities in terms of sensitivity, enabling it to handle a diverse range of tasks. These range from manipulating fragile items, necessitating high sensitivity, to lifting heavy objects where relatively lower sensitivity suffices. Given the fact that sensitivity and measurement range are typically inversely related, a rise in sensitivity usually results in a reduced measurement range. Reducing the overall measurement range by enhancing the softness of the sensing information route is advantageous [3], as it aligns with the goal of increasing sensitivity, particularly useful for handling fragile objects. Notably, a softer sensor has a greater capacity to conform to and handle delicate objects gently.

In humans, it has been demonstrated that modulating the physical properties of the body can enhance proprioceptive feedback [4]. Similarly, innovations in soft actuators have led to significant advancements in robotic grasping capabilities by actively altering their shape, and these actuators leverage variable elasticity to improve robust grasping[5], [6]. Building on these insights, a key research direction is the development of robotic tactile sensors that integrate actuation. These sensors can adjust the internal impedance of the robot's physical structure, thereby enhancing sensing quality in response to the specific dynamics of the task at hand. Additionally, due to frequent contact with the environment, the robotic skin is more prone to damage compared to other parts of the robot. Consequently, it is crucial that damaged sections of the skin can be easily fabricated and replaced [7].

In this study, we introduce a tactile sensor whose sensitivity and compliance can be dynamically altered by controlling the air pressure in its cavity structure. Furthermore, its streamlined design simplifies the manufacturing process.

The remainder of this paper is organized as follows. Section II presents a review of existing tactile sensors. The proposed tactile sensor is then introduced in Section III. Section IV describes the setup and results of the experiments. Finally, the conclusions and future works are provided in Section V.

II. Relatead Works

Tactile sensors operate based on various principles, including resistive [8], capacitive [9], piezoelectric [10], optical [11], and magnetic [12] mechanisms. Each of these methods has been thoroughly explored. Particular attention has been given to magnetic sensors for their ability to sense along three axes with a simple structural design [13], [14], [15]. Optical sensors, as referenced in [16], [17], [18], also facilitate 3-axis sensing. However, their bulky size limits installation in compact spaces, and they are computationally resource-consuming. The sensors mentioned above cannot adjust either sensitivity or compliance. There are adjustable sensors, like those cited in [19], [20]; their adjustability is achieved through offline material modification, rendering them unable to handle dynamic situations effectively. In-situ sensor adjustment requires on-the-fly modification. As seen in [21], [22], 3-axis sensing is enabled by the use of 3D magnetic transducers, with sensor adjustment achieved by

*These authors contributed equally
Devesh Abhyankar, Yushi Wang, Shigeki Sugano, and Mitsuhiro Kamezaki are with the Department of Modern Mechanical Engineering, Research Innovation Center, Waseda University, Tokyo 162-0041, Japan
Yuhiro Iwamoto is with the Department of Electrical and Mechanical Engineering, Nagoya Institute of Technology, Gokiso-cho, Showa-ku, Nagoya, Aichi, 466-8555 Japan
Mitsuhiro Kamezaki is with the Graduate School of Engineering, The University of Tokyo, 7-3-1 Hongo, Bunkyo-ku, Tokyo 113-8656, Japan
Corresponding author: devesh@fuji.waseda.jp

varying the magnetic field generated by current applied to one or more coils. However, incorporating coils at the contact point introduces safety concerns. In addition to electrical adjustment, mechanical adjustment methods have also been studied, as discussed in [23], [5]. The variation in air pressure changes the stiffness of the sensors, thereby influencing the sensitivity of the sensing units. The implementation of a pneumatic method for both pressure modulation and sensing enables real-time adjustments in sensitivity. However, this approach confines their sensing capabilities to a single direction. Adjustable sensors with 3-axis sensing also exist as in [24], [25]. The integration of pneumatics for mechanical shape modulation and optics for 3-axis sensing demonstrates a design strategy that enhances sensing capabilities under variable conditions while preserving rich contact information.

However, this approach inherits the same limitations associated with optical sensors, as previously mentioned. Pneumatics combined with magnetics has also been proposed in[26]. Using a hard magnet decreased the sensor's overall compliance, and embedding the magnet into the silicone necessitated high precision, leading to a more complex manufacturing process. In light of recent advancements in material science and technology, Permanent Magnet Elastomer (PME) has been introduced [7], [15], [27], [28]. This elastomer, known for its high magnetic remanence and elasticity, is well-suited for integration into pneumatic systems. The proposed sensor adopts this material to achieve adjustable sensitivity and compliance.

III. Sensor Prototype

A. Sensor design

The proposed sensor integrates the three-dimensional sensing capabilities of magnetic sensors with the adjustability offered by pneumatic sensors, as shown in Fig. 1. Featuring an extremely simple design, it incorporates Permanent Magnet Elastomer (PME), known for its strong magnetic remanence and elasticity, along with a stiffer silicone base to form a closed cavity. The deformation of this sensor during interaction with the environment is related to its internal stresses. By altering the internal air pressure, the sensor's characteristics, particularly compliance and measuring range, can be dynamically modulated. This concept is elucidated in Section I, where the correlation between measuring range and sensitivity is discussed.

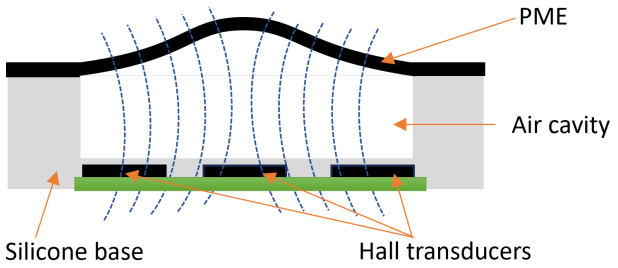

Fig. 1. Concept of the sensor design.

B. Sensor manufacture

Fig. 2 shows the manufacturing processes and assembled prototype of the sensor. Designed with simplicity to facilitate ease of fabrication, the sensor's structure incorporates PME as the inflatable sensing element. Silicone-Silpot 184 (Shore Hardness: 43A), is selected to be the stiffer base part, allowing only the PME side to inflate. A cavity was intentionally created on the base side of the sensor to simplify the integration of the pneumatic system through an air inlet. As displayed in Fig. 2, the fabrication process comprises two primary components corresponding to the sensor's main structure: the PME and the base. The PME is fabricated by blending NdFeB particles with a diameter of 20 µm into Ecoflex 50 silicone (Shore Hardness: 00-50). This mixture is then cast into a mold, forming a layer with dimensions of 2 mm in thickness and 66 mm in diameter. Following curing, the PME is subjected to a powerful electromagnetic field, magnetizing it and achieving a remanence on its surface as high as 45 mT. The base is constructed using Silpot 184, poured into a specially designed mold with a cap for creating the cavity. Additionally, a Printed Circuit Board (PCB) is designed to be mounted on the base. To ensure seamless integration, the base mold replicates the pattern of the PCB on its bottom side.

IV. Sensor Characterization

In this section, a series of experiments were conducted. Firstly, sensitivity evaluation experiments measured the magnetic field's change in response to applied forces at various pressure levels. Secondly, compliance evaluation experiments assessed the sensor's deformation distance under external forces subjected to differing pressures. Then, the sensor was calibrated in three axes using linear regression. Additionally, the sensor's hysteresis and signal-to-noise ratio (SNR) under various pressure levels were evaluated.

A. Experimental setup

The experimental setup utilized in this study is depicted in Fig. 3. The sensor is positioned on a motorized XY-axis stage (KYS18100-N10-JK, Suruga Seiki) that has an operational accuracy of 0.02 mm and a movement speed of 0.04 mm/sec. To exert external forces, a disk-shaped indentor (diameter: 55 mm and thickness: 3 mm) was affixed to a 6-axis force/torque sensor (LGR101U, Leptrino, 1.2 kHz). This sensor, integral for monitoring applied forces, was connected to the UR5e robot arm's end-effector via a custom 3D-printed adapter. An industrial Micro laser distance sensor (HG-C110, Panasonic Industry) was also mounted on the UR5e arm using the same adapter, providing precise compliance measurements.

The pneumatic system employed for pressure control is shown in Fig. 4. This system comprises an air pump (ZR320-02PM, Adafruit), a three-port solenoid valve (VT307-5D1-02-F, SMC), a relief valve, and a pressure sensor (U5244-000005-030PA, TE-Connectivity). The integration of these components enables air pressure regulation within the system with a resolution of 0.04 PSI. For data acquisition, an NXP LPC1768 microcontroller was employed, collecting

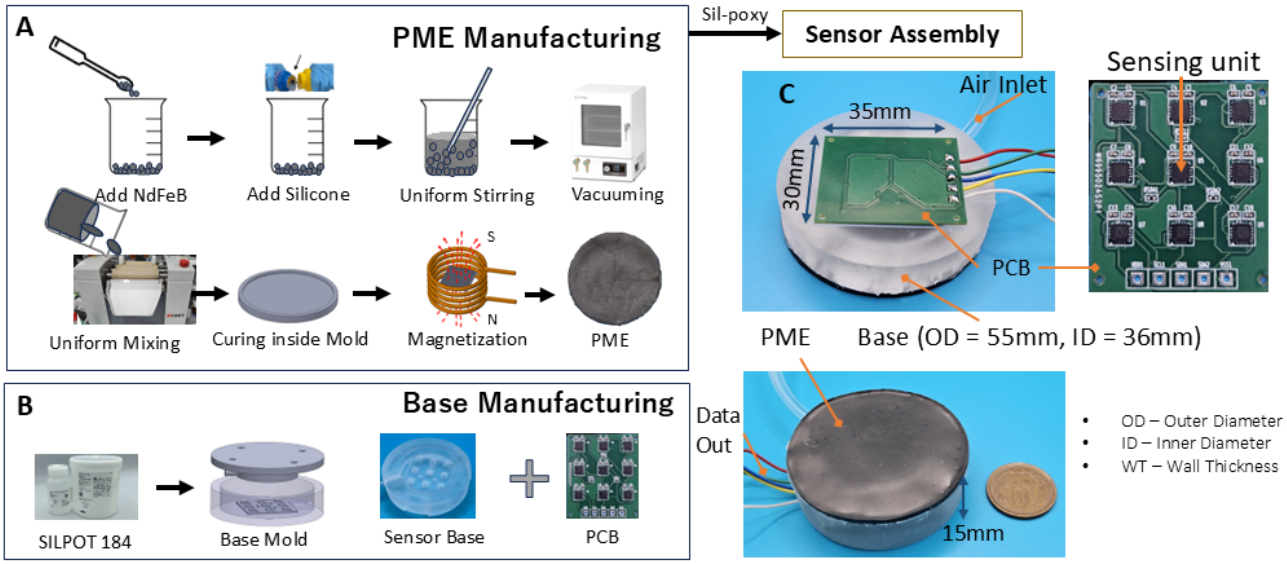

Fig. 2. Sensor manufacturing processes. A) Fabrication of the PME: NdFeB powders and Ecoflex 50 are mixed in a 50% weight ratio. This mixture is subjected to a 20-minute vacuum treatment to eliminate air bubbles. Subsequently, it undergoes further homogenization in a roller mill. The resulting blend is then poured into a mold and left to cure at room temperature for 24 hours. After Post-curing, the elastomer is magnetized using an electromagnet, thereby completing the PME fabrication. B) Production of the Base: Silpot 184 is cast into the specially designed base mold and cured for 5 hours at 70 °C. A PCB, dimensioned 30 X 35 mm and featuring 9 transducers arranged in a 3 X 3 grid, is then integrated into the base. C) After using Sil-poxy to paste the PME and base together, a Vinyl tube is attached to the base as the air inlet of the cavity.

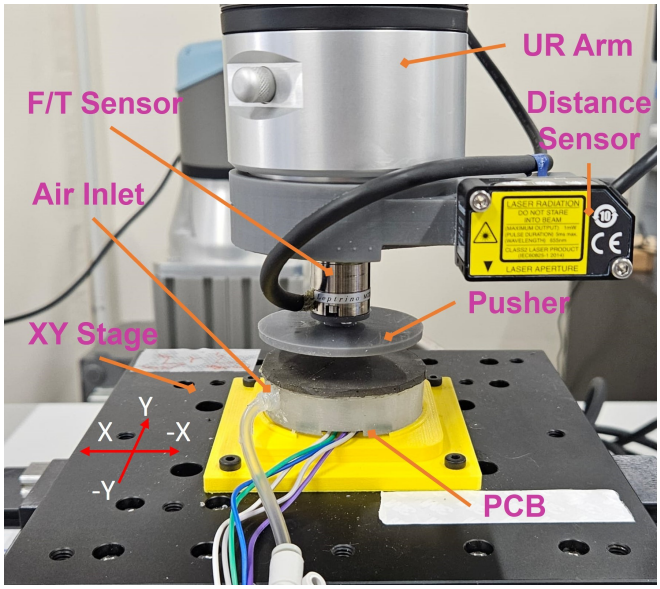

Fig. 3. Experimental setup.

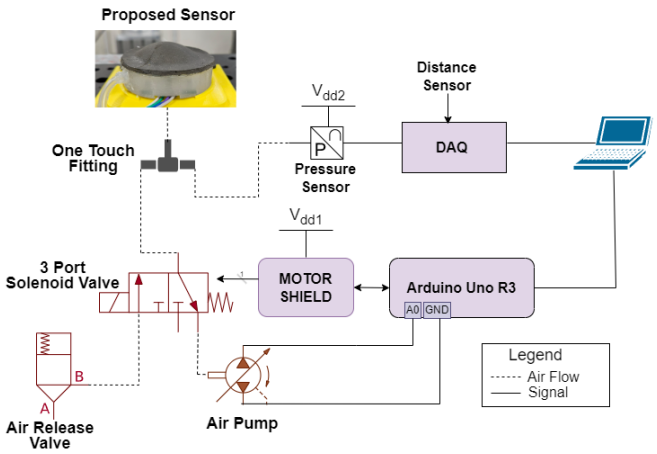

Fig. 4. Pneumatic control system.

magnetic field data from Hall sensors. These sensors were configured to output data in burst mode at a frequency of 500 Hz. The study primarily focused on the center hall sensor as shown in Fig. 2 as the representative sensing unit for all experiments. This unit, situated at the sensor module's center and the highest point of the dome shape created by the inflated PME, is optimally placed for capturing magnetic field variations under different pressure levels. In the future, we will use the whole matrix to enhance sensor capabilities like contact point location estimation and shape recognition application as the other units will enhance the spatial resolution. Data from both the pressure sensor and the laser distance sensor were gathered using a NI USB 6212 (National Instruments, TX). Further elaboration on the experiment's details and methodologies is provided in the respective subsections dedicated to each experiment.

B. Adjustable sensitivity

For measuring devices, sensitivity is the ratio of the magnitude of its response to the magnitude of the quantity measured [29]. Similar to [30], in our work, sensitivity is defined as the ratio of the change in magnetic field to the

force that caused this change, as described in

$$S = \frac{\Delta B}{\Delta F} \tag{1}$$

where S denotes the sensitivity of our tactile senor, B represents the magnetic field, and F is the force measured. In this experiment, the variation in the magnetic field was analyzed in response to external forces applied at different pressure levels. The experiment aimed to determine the maximum applicable forces and sensitivity, and the sensor was indented in a stepwise manner up to its maximum limit. The PME was inflated to five distinct pressure values: 15.0, 15.2, 15.4, 15.6, and 15.8 PSI. Forces ranging from 0 N to the maximum value were applied in 1 N increments. Please note that the pressure measurements presented in this study are expressed in PSI (pounds per square inch), as obtained directly from the sensor utilized in our experimental setup. For reader convenience, the conversion formula from PSI to pascals is provided as follows: $1\ \text{PSI} = 6.895\ \text{kPa}$. To determine the maximum force at each pressure level, the PME was pressed until it became completely flat, ensuring full contact of the indenter with the elastomer surface. Before force application, the PME was inflated to the target pressure, monitored by an air pressure sensor. The UR arm was then calibrated for 1-N step changes using the force sensor. In the program, each force increment was maintained for 3 seconds. The UR arm's initial position, corresponding to the 0-N step, remained constant across all pressure levels. During each trial, data from the Hall sensor, force sensor, pressure sensor, and distance sensor were recorded. Three trials were conducted for each pressure level. Following the completion of trials at a given pressure, the sensor was deflated and allowed to rest for several hours so that it returned to its initial state.

The results are shown in Figs. 5–7. In the Z-axis, a positive correlation exists between the applied force and magnetic field intensity, attributed to the PME getting nearer to the transducer under force. Further, each 1 N of force results in notably smaller increases in the magnetic field as the pressure increases. In contrast, the X- and Y-axes display a negative proportional relationship between the magnetic field and displacement, owing to shear-direction movements driving the center of PME further from the transducer. Similarly, increased pressure leads to a decreased magnetic field change for the same displacement. There is a slight difference in the strength of the X- and Y-axes magnetic field due to the inhomogeneity of NdFeB distribution and the variation in the thickness of the sheet. In conclusion, the increased pressure resulted in reduced sensitivity in all three axes, as listed in Table I.

C. Adjustable compliance

As it is difficult to measure compliance directly, we relate it to the deformation change that the sensor undergoes at different pressure levels as illustrated in Fig. 8. To obtain the deformation change, we first measured the distance D (mm) end-effector travels under all three pressure levels

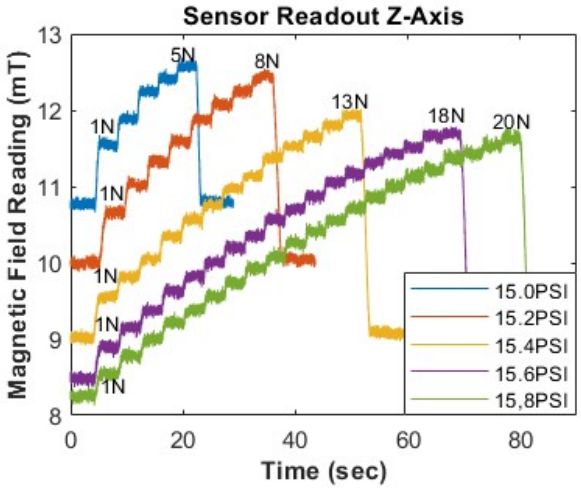

Fig. 5. Magnetic field change in response to external forces (sensitivity) in Z-axis when subject to various pressures.

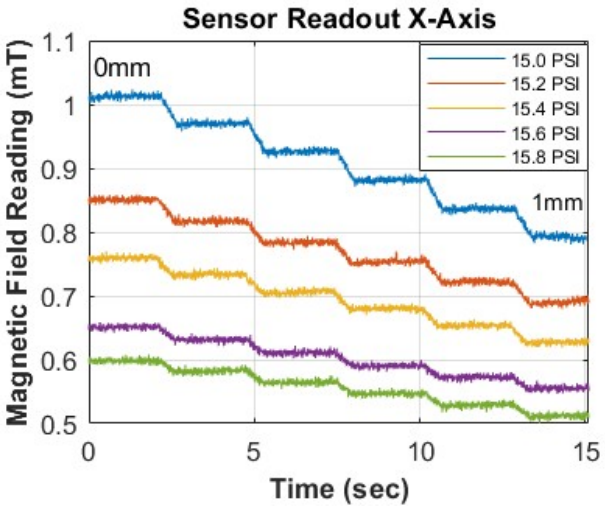

Fig. 6. Magnetic field change in response to external forces (sensitivity) in X-axis when subject to various pressures.

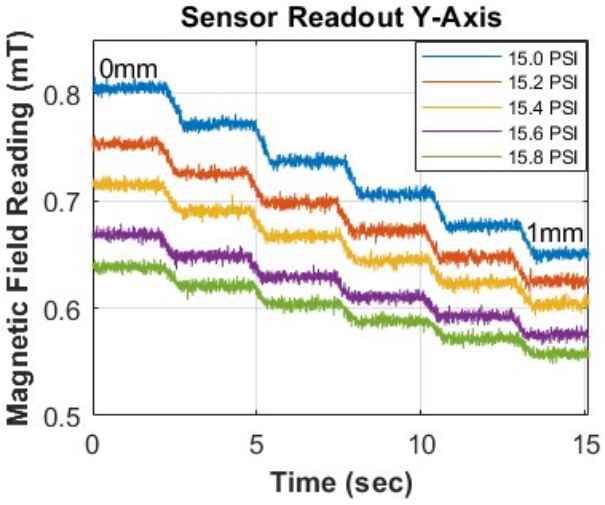

Fig. 7. Magnetic field change in response to external forces (sensitivity) in Y-axis when subject to various pressures.

TABLE I. SENSITIVITY OF EACH AXIS UNDER DIVERSE PRESSURES

Pressure (PSI)	Sensitivity (mT/N)		
	X	Y	Z
15.0	0.125	0.13	0.45
15.2	0.117	0.117	0.349
15.4	0.109	0.108	0.242
15.6	0.098	0.093	0.188
15.8	0.093	0.089	0.169

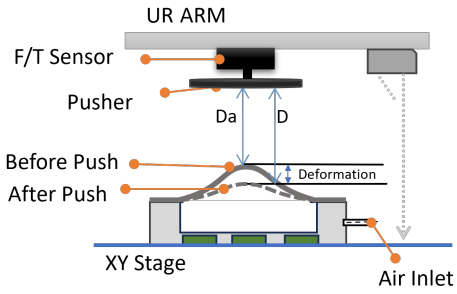

Fig. 8. Illustration of adjustable compliance experiment.

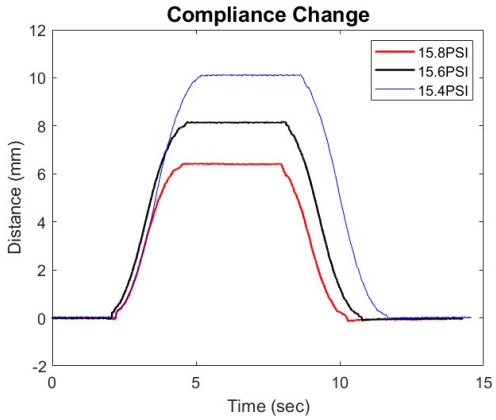

Fig. 9. Distance traveled by end-effector for 1 N push at 15.4, 15.6, and 15.8 PSI pressure level.

TABLE II. SENSOR DEFORMATIONS UNDER DIFFERENT PRESSURES

Air Pressure (PSI)	D (mm)	Da (mm)	Deformation (mm)
15.0	10.19	6.40	3.79
15.4	8.31	4.95	3.36
15.8	6.60	3.40	3.20

when the proposed sensor was pushed for 1 N and kept for 3 seconds. The initial position of the end-effector was fixed for all pressure levels. The distance the end-effector traveled is shown in Fig. 9. Since the distance D under each pressure will also include the distance traveled in the air, i.e., until it touches the sensor surface, we subtracted the distance traveled in the air Da (mm) from the total distance change D (mm). The distance Da (mm) is calculated using the distance sensor before the experiment. The results are summarized in Table II. With a consistent force applied, the deformation of the proposed sensor decreases as internal air pressure rises, reflecting compliance changes induced by pneumatic control.

D. Sensor calibration

Data was collected by applying forces in the Z-axis (normal force) and the X- and Y-axes (shear force) stepwisely. Z-axis force was applied from 0–5 N with a 1 N step size using the flat disk-shaped pusher (diameter: 55 mm) attached to the end-effector of the UR arm. The steps were set by monitoring the force reading from the reference force/torque (F/T) sensor; each force was applied for 3 seconds. To generate shear forces, first, a normal force of 4 N was applied to the proposed sensor. Then, under the constant normal force of 4 N, a loading and unloading cycle was created by moving the XY stage. The stage was moved from 0–1 mm in 5 steps in the +X direction with each step of 0.2 mm and returned back to 0 mm along the same steps. Each step lasted for 2 seconds. Further, the stage was moved in the -X direction with the same step size and distance. After the stage returned to the initial (0 mm position), the normal force of 4 N was also unloaded. Similarly, this was done for the Y-axis in both directions, the +Y and -Y. To synchronize both sensors, we recorded Unix timestamps for each dataset and then compared them. The matching timestamps were used to get the synchronized values for both the proposed PME sensor and the F/T sensor.

1) Model training: To calibrate the digital readings of the Hall sensor for the force value, we used the MATLAB Regression Learner App from the Statistics and Machine Learning Toolbox. The data collected above after synchronization was used as training data. The plots for the same are given in Figs. 10 (a)–(c). In all the plots, the y-axis represents the change in magnetic field from the initial value when no force was applied. It is observed that while calibrating one axis, the magnetic fields in other two axes also vary. This is due to cross-talk between axes, and we will explore ways to compensate for it in future works. In the training data, ΔB_x, ΔB_y, and ΔB_z are the predictors, and the force reading for the corresponding axis is the response variable. We used a linear regression model. The model summary is given in Table III. Our goal is not to find out the best calibration model but to validate the 3-axis sensing of the adjustable tactile sensor. In the future, we will use and compare different models to improve the sensor performance.

2) Model prediction: To validate the developed model, an external set of forces, distinct from those employed in the training phase, was utilized as a testing dataset. Specifically, for the Z-axis, forces of [0, 1.5, 2.5, 3.5, 4.5, 5] N were applied. In the case of shear forces, the stage underwent controlled movements spanning distances of [0, 0.25, 0.50, 0.75, 0.5, 0.25, 0] mm, executed in both the +X and +Y directions. Upon reaching the zero position, this identical movement pattern was replicated in reverse, for the -X and -Y directions. The Root Mean Square Error (RMSE) obtained for the test data for all three axes is summarized in Table IV. These findings exhibit the linear response of our sensor and that simple linear regression can be used

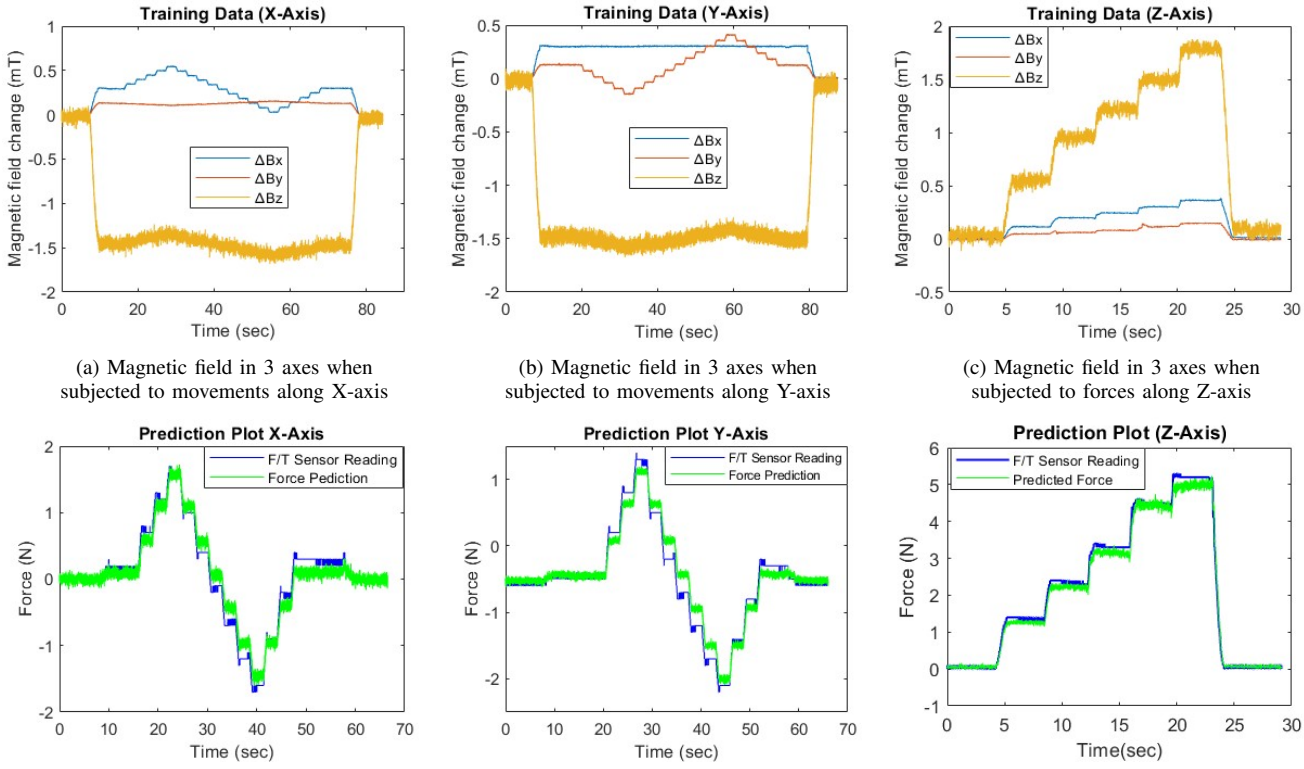

(a) Magnetic field in 3 axes when subjected to movements along X-axis

(b) Magnetic field in 3 axes when subjected to movements along Y-axis

(c) Magnetic field in 3 axes when subjected to forces along Z-axis

(d) Force prediction in X-axis

(e) Force prediction in Y-axis

(f) Force prediction in Z-axis

Fig. 10. The overlap between force prediction and reference sensor measurement. The results indicate that calibration of forces along the three axes is feasible.

TABLE III. GOODNESS OF FIT STATISTICS

Axis	Regression	RMSE (N)	R square
Z	Linear	0.134	0.994
X	Linear	0.21	0.95
Y	Linear	0.21	0.95

TABLE IV. RMSE OF CALIBRATION MODEL OF EACH AXIS

Axis	RMSE (N)
X	0.15
Y	0.14
Z	0.20

to calibrate our sensor. While future enhancements might include the adoption of neural networks, such explorations extend beyond the scope of the current paper.

E. Hysterisis

Hysteresis, characterized by a lag or delay in response, is generated during the loading and unloading cycle due to the presence of viscoelastic material. In our case, this material is the Ecoflex 50 silicone used to make the PME film. To assess the impact of pressure changes on hysteresis, we conducted tests under two distinct pressure conditions, i.e., 15.0 and 15.8 PSI, covering all three axes. In this experiment, the sensor underwent a series of load and unload cycles on the Z-axis, employing five force levels. Each force, incrementing in steps of 1 N, was sustained for 3 seconds, reaching a maximum applied force of 5 N. For the X- and Y-axes, a constant normal force of 2 N was applied, then the X-Y stage was programmed for bidirectional movement: it progressed linearly from 0 to 1 mm and then reversed its course. This movement was executed in increments of 0.2 mm, with a waiting period of 2 seconds at each step. To calculate the hysteresis, we used the following formula

$$Hysteresis\% = \frac{F_{mu} - F_{ml}}{F_{max} - F_{min}} \times 100\%, \qquad (2)$$

where F_{mu} is the maximum force measured by the proposed sensor at the midpoint of the force readings provided by the force/torque (F/T) sensor, and F_{ml} is the minimum force measured by the proposed sensor at the same midpoint. F_{max} and F_{min} represent the maximum and minimum forces measured by the F/T sensor, respectively.

The results for the three axes are plotted in Fig. 11 and summarized in Table V. Observations indicate a reduction in hysteresis across all three axes when the air pressure within the sensor cavity is set to 15.80 PSI. This phenomenon is attributed to the decreased deformation of the PME at higher air pressures, in contrast to the more pronounced deformation

TABLE V. 3-AXES HYSTERESIS RESULTS

Axis	Hysteresis (15.00 PSI)	Hysteresis (15.80 PSI)
X	13.80%	5.82%
Y	12.62%	8.90%
Z	4.02%	2.94%

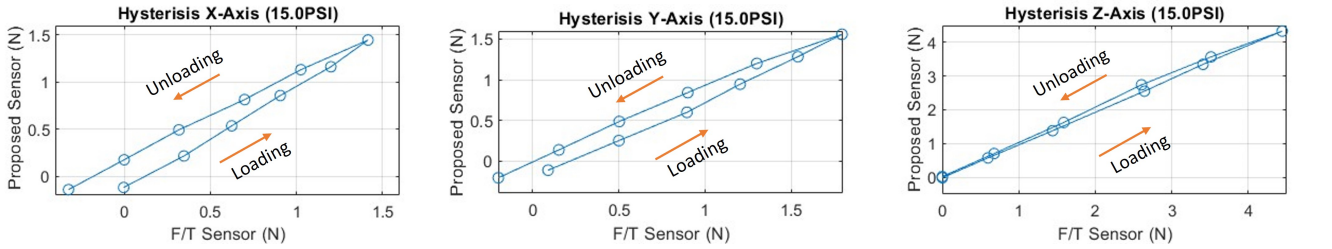

(a) X-axis cyclical force (15.0 PSI) (b) Y-axis cyclical force (15.0 PSI) (c) Z-axis cyclical force (15.0 PSI)

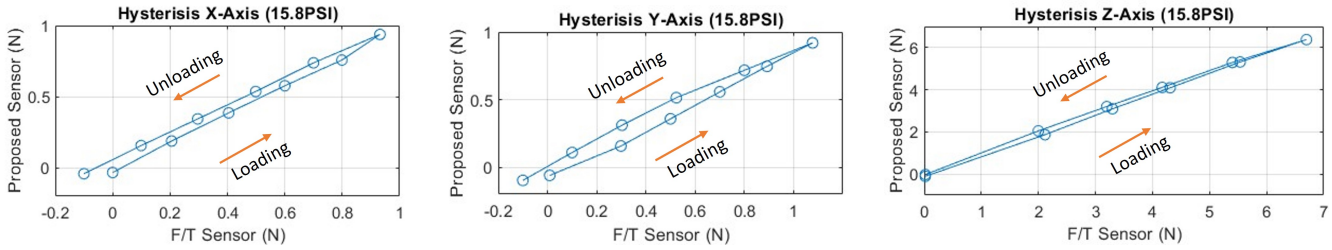

(d) X-axis cyclical force (15.8 PSI) (e) Y-axis cyclical force (15.8 PSI) (f) Z-axis cyclical force (15.8 PSI)

Fig. 11. Hysteresis in three axes at different pressures.

TABLE VI. SNR COMPARISON FOR DIFFERENT AIR PRESSURES

Pressure (PSI)	SNR
15.0 (PSI)	34.52
15.2 (PSI)	37.19
15.4 (PSI)	37.90
15.6 (PSI)	38.56
15.8 (PSI)	39.23

observed at lower pressures. This observation is consistent with the trend of reduced compliance at higher air pressures, as seen in the adjustable compliance experiments.

F. Signal-to-noise ratio (SNR)

From the previous experiment results of adjustable sensitivity for the Z-Axis, the SNR was calculated using the equation given below.

$$\mathrm{SNR}_{\mathrm{dB}} = 20\log_{10}\left(\frac{|\mu-\mu_0|}{\sigma_0}\right)\mathrm{dB} \tag{3}$$

where μ is the mean of the sensing unit measurements when the proposed sensor is loaded, μ_0 is the mean of the sensing unit measurements when the proposed sensor is not loaded, and σ_0 is the standard deviation when the proposed sensor is not loaded. The results are summarized in Table VI. It was found that increasing the air pressure results in a higher value of SNR.

V. CONCLUSION AND FUTURE WORKS

A. Conclusion

This study introduces a novel 3-axis tactile sensor, characterized by its dynamically adjustable compliance. This adjustability is achieved by modulating the air pressure within the sensor's cavity structure, altering its physical properties. Consequently, this modification results in changes in sensitivity (or measuring range) across all three axes. Experimental data demonstrate a range of sensitivity variations from 0.093 to 0.125 mT/N, 0.089 to 0.13 mT/N, and 0.169 to 0.45 mT/N in the X-, Y-, and Z-axes, respectively. The compliance modulation was examined by applying a 1 N force under various pressure levels while measuring the distance the indentor traveled, with the results indicating that at higher pressure, the proposed sensor deforms less under the same force. Furthermore, the sensor's efficacy as a 3-axis device was validated by employing a linear regression model to deduce forces along three axes from the measured magnetic fields. Additionally, the impact of pressure change on the hysteresis of this soft tactile sensor was assessed. The findings show that at lower pressures, there is a higher hysteresis across all three axes. Finally, testing of the sensor's SNR revealed that increasing the softness leads to a reduction in SNR.

This sensor with such adjustable compliance and sensitivity contributes to increase the adaptability of the robot to uncertainties by allowing it to vary its mechanical and sensing characteristics dynamically. Moreover, the capability of active sensing facilitates diverse interaction paradigms with the environment. A prime example of this application is palpation, akin to the method employed by medical professionals. Physicians adjust the stiffness of their fingers to obtain optimized haptic information, a process that can be replicated effectively by the proposed sensor in robotic systems.

B. Future works

In the future, several improvements can be done for our sensor design. A key enhancement is the reduction of sensor thickness. This adjustment is feasible due to the initial design of the sensor's base thickness, which was tailored to accommodate the size of the air inlet located on its side. A redesign method would involve relocating the air inlet from the side to the bottom, or incorporating an additional

structure. This change would allow the height of the air cavity to be minimized to zero when not inflated. The manufacturing methodology of PME also needs to be improved to obtain a homogeneous distribution of NdFeB particles and uniform thickness throughout the sheet. The current design necessitates a pneumatic system for activation. To streamline integration, it is advisable to install this sensor on robots that are already pneumatically driven, leveraging their existing pneumatic source. This approach would eliminate the need for separate air pumps. Furthermore, the sealing robustness requires enhancement. The present configuration is unable to withstand air pressures exceeding 15.80 PSI. To address this, the use of stronger adhesives is recommended, which would ensure a more reliable seal under higher pressure conditions. Lastly, as a magnetic sensor, it's important to note that interacting with ferromagnetic materials can interfere with magnetic readings, resulting in unreliable force measurements. Therefore, incorporating magnetic shielding is essential to ensure accurate and consistent sensor performance.

ACKNOWLEDGMENT

This work is supported by JSPS KAKENHI Grant Numbers 22K17980 and 23H01381, and also by the Research Institute Science and Engineering and the Future Robotics Organization, Waseda University.

REFERENCES

[1] Y. Hu, Q. Xie, V. Jain, J. Francis, J. Patrikar, N. Keetha, S. Kim *et al.*, "Toward general-purpose robots via foundation models: A survey and meta-analysis," 2023, arXiv preprint arXiv:2312.08782.

[2] H. Wang, M. Totaro, and L. Beccai, "Toward perceptive soft robots: Progress and challenges," *Advanced Science*, vol. 5, no. 9, p. 1800541, 2018. [Online]. Available: https://dx.doi.org/10.1002/advs.201800541

[3] A. Mohammadi, Y. Tan, P. Choong *et al.*, "Flexible mechanical metamaterials enabling soft tactile sensors with multiple sensitivities at multiple force sensing ranges," *Scientific Reports*, vol. 11, p. 24125, 2021.

[4] R. S. Johansson and Å. B. Vallbo, "Tactile sensory coding in the glabrous skin of the human hand," *Trends in Neurosciences*, vol. 6, pp. 27–32, 1983.

[5] L. He, Q. Lu, S.-A. Abad, N. Rojas, and T. Nanayakkara, "Soft fingertips with tactile sensing and active deformation for robust grasping of delicate objects," *IEEE Robotics and Automation Letters*, vol. 5, no. 2, pp. 2714–2721, 2020.

[6] F. Ilievski, A. D. Mazzeo, R. F. Shepherd, X. Chen, and G. M. Whitesides, "Soft robotics for chemists," *Angewandte Chemie International Edition*, 2011.

[7] R. Bhirangi, T. Hellebrekers, C. Majidi, and A. Gupta, "Reskin: versatile, replaceable, lasting tactile skins," *arXiv preprint arXiv:2111.00071*, 2021. [Online]. Available: https://arxiv.org/abs/2111.00071

[8] K. Weiß and H. Worn, "The working principle of resistive tactile sensor cells," in *IEEE International Conference Mechatronics and Automation, 2005*, vol. 1. IEEE, 2005, pp. 471–476.

[9] H.-K. Kim, S. Lee, and K.-S. Yun, "Capacitive tactile sensor array for touch screen application," *Sensors and Actuators A: Physical*, vol. 165, no. 1, pp. 2–7, 2011.

[10] K. Noda, K. Hoshino, K. Matsumoto, and I. Shimoyama, "A shear stress sensor for tactile sensing with the piezoresistive cantilever standing in elastic material," *Sensors and Actuators A: Physical*, vol. 127, no. 2, pp. 295–301, 2006.

[11] R. Li and E. H. Adelson, "Sensing and recognizing surface textures using a gelsight sensor," in *Proceedings of the IEEE Conference on Computer Vision and Pattern Recognition*, 2013, pp. 1241–1247.

[12] H. Wang, G. De Boer, J. Kow, A. Alazmani, M. Ghajari, R. Hewson, and P. Culmer, "Design methodology for magnetic field-based soft tri-axis tactile sensors," *Sensors*, vol. 16, no. 9, p. 1356, 2016.

[13] D. S. Chathuranga, Z. Wang, Y. Noh, T. Nanayakkara, and S. Hirai, "Magnetic and mechanical modeling of a soft three-axis force sensor," *IEEE Sensors Journal*, vol. 16, no. 13, pp. 5298–5307, 2016.

[14] S. Shembekar, M. Kamezaki, P. Zhang, Z. He, Y. Iwamoto, Y. Ido, H. Sakamoto, and S. Sugano, "Development of a permanent magnet elastomer (pme) infused soft robot skin for tactile sensing," in *2021 IEEE/RSJ International Conference on Intelligent Robots and Systems (IROS)*. IEEE, 2021, pp. 6039–6046.

[15] Y. Wang, M. Kamezaki, Q. Wang, H. Sakamoto, and S. Sugano, "3-axis force estimation of a soft skin sensor using permanent magnetic elastomer (pme) sheet with strong remanence," in *2022 IEEE/ASME International Conference on Advanced Intelligent Mechatronics (AIM)*, 2022, pp. 302–307.

[16] B. Ward-Cherrier, N. Pestell, L. Cramphorn, B. Winstone, M. E. Giannaccini, J. Rossiter, and N. F. Lepora, "The tactip family: Soft optical tactile sensors with 3d-printed biomimetic morphologies," *Soft Robotics*, vol. 5, no. 2, pp. 216–227, 2018.

[17] A. Yamaguchi and C. G. Atkeson, "Combining finger vision and optical tactile sensing: Reducing and handling errors while cutting vegetables," in *2016 IEEE-RAS 16th International Conference on Humanoid Robots (Humanoids)*. IEEE, 2016, pp. 1045–1051.

[18] A. Yamaguchi and C. G. Atkeson, "Implementing tactile behaviors using fingervision," in *2017 IEEE-RAS 17th International Conference on Humanoid Robotics (Humanoids)*, Birmingham, UK, 2017, pp. 241–248.

[19] X. Wang, J. Li, H. Song, H. Huang, and J. Gou, "Highly stretchable and wearable strain sensor based on printable carbon nanotube layers/polydimethylsiloxane composites with adjustable sensitivity," *ACS Applied Materials Interfaces*, vol. 10, no. 8, pp. 7371–7380, 2018.

[20] M. Amjadi, A. Pichitpajongkit, S. Lee, S. Ryu, and I. Park, "Highly stretchable and sensitive strain sensor based on silver nanowire–elastomer nanocomposite," *ACS Nano*, vol. 8, no. 5, pp. 5154–5163, 2014.

[21] A. C. Holgado, J. A. A. Lopez, T. P. Tomo, S. Somlor, and S. Sugano, "Improvements on a sensitivity adjustable 3-axis soft skin sensor with an electromagnet," in *2020 IEEE/SICE International Symposium on System Integration (SII)*. IEEE, 2020, pp. 68–73.

[22] S. Xie, Y. Zhang, H. Zhang, and M. Jin, "Development of triaxis electromagnetic tactile sensor with adjustable sensitivity and measurement range for robot manipulation," *IEEE Transactions on Instrumentation and Measurement*, vol. 71, pp. 1–9, 2022.

[23] G. Pang, G. Yang, W. Heng, Z. Ye, X. Huang, H.-Y. Yang, and Z. Pang, "Coboskin: Soft robot skin with variable stiffness for safer human–robot collaboration," *IEEE Transactions on Industrial Electronics*, vol. 68, no. 4, pp. 3303–3314, 2020.

[24] A. Goncalves, N. Kuppuswamy, A. Beaulieu, A. Uttamchandani, K. M. Tsui, and A. Alspach, "Punyo-1: Soft tactile-sensing upper-body robot for large object manipulation and physical human interaction," in *2022 IEEE 5th International Conference on Soft Robotics (RoboSoft)*. IEEE, 2022, pp. 844–851.

[25] S. Joonhigh, N. Kuppuswamy, A. Beaulieu, A. Alspach, and R. Tedrake, "Variable compliance and geometry regulation of soft-bubble grippers with active pressure control," in *2021 IEEE 4th International Conference on Soft Robotics (RoboSoft)*. IEEE, 2021, pp. 169–175.

[26] S. Azim, A. Srinivasan, M. Pandaram, J. Kow, G. De Boer, H. Wang, A. Alazmani, and P. Culmer, "Soft tactile sensors with variable compliance," in *2017 IEEE SENSORS*. IEEE, 2017, pp. 1–3.

[27] D. Abhyankar, Y. Wang, M. Kamezaki, Q. Wang, and S. Sugano, "Preliminary study on the feasibility of using permanent magnetic elastomer as a stretchable skin sensor," in *2024 IEEE/SICE International Symposium on System Integration (SII)*. IEEE, 2024, pp. 526–531.

[28] H. Enomoto, M. Ishige, T. Umedachi, M. Kamezaki, and Y. Kawahara, "Delicate jamming grasp: Detecting deformation of fragile objects using permanent magnet elastomer membrane," *IEEE Robotics and Automation Letters*, vol. 9, no. 2, pp. 979–986, 2024.

[29] J. R. Vig and F. L. Walls, "A review of sensor sensitivity and stability," in *Proceedings of the 2000 IEEE/EIA International Frequency Control Symposium and Exhibition*. IEEE, Jun. 2000, pp. 30–33, cat. No. 00CH37052.

[30] G. Pang, J. Deng, F. Wang, J. Zhang, Z. Pang, and G. Yang, "Development of flexible robot skin for safe and natural human–robot collaboration," *Micromachines*, vol. 9, no. 11, p. 576, 2018.